Nanoscale Advances

ROYAL SOCIETY OF CHEMISTRY

COMMUNICATION

View Article Online
View Journal | View Issue

Cite this: *Nanoscale Adv.*, 2022, **4**, 2782

Received 18th April 2022
Accepted 9th May 2022

DOI: 10.1039/d2na00233g

rsc.li/nanoscale-advances

Concave octopus-like PtCu nanoframe mediated photo-electro Fenton catalysis for fast organic dyestuff elimination†

Yangyang Yan,‡[ab] Shaowen Cheng,‡[a] Ping Zhou,[a] Heying Li,[ab] Xiaoran Liu,[a] Manping Lin,[a] Feihu Xie,[b] Keke Zhang,*[b] Yi Zhang,[b] Chenyang Zhang,[b] Shuang Zhao,[c] Jiahua Shi *[c] and Jinghua Li *[abc]

In this work, a photo-electro Fenton catalytic nanoplatform based on concave octopus-like PtCu nanoframes was fabricated for organic dyestuff degradation. The electrochemical oxidation reaction was performed to generate hydrogen peroxide (H_2O_2) on the interface of PtCu nanoframes *via* a promising electro-Fenton process for on-demand aqueous remediation.

With the fast development of industrialization and modern urbanization, dyestuff-containing wastewater will cause a variety of environmental problems due to its potential physiological toxicity such as teratogenic risk, mutagenicity, sensitization and oncogenicity,[1,2] which could induce many disasters to aquatic ecosystems or even result in grievous health risks to people.[3,4] So it is necessary to reinforce efficient strategies for dyestuff wastewater treatment.[5,6] Recently, numbers of physicochemical formulae have been advanced to adsorb/degrade harmful dyes from colored effluents. The operating methods include physisorption, barrier separation, flocculation, coprecipitation, reverse osmosis, chemical oxidation, biodegradation, *etc.*[7–11] However, some of these executable techniques are too expensive, highly energy-consuming, cumbersome to operate and excessively time consuming.[12] All these deficiencies restrict the functionality available for water purification applications and organic pollutant treatment.[13] More effective endeavors are needed for the research and development necessary to develop new strategies for resolving environmental problems.

Nowadays, advanced oxidation strategies (AOSs) have served as high-performance technologies for organic dyestuff degradation.[14,15] Methods such as the ultrasonic catalysis, ozone treatment, photochemical catalysis, metallocene catalysts, electrodeposition, Fenton catalysis, photo-Fenton process, and electro-Fenton method have displayed an outstanding performance in dye removal.[16–18] Especially, the photo-electro Fenton maneuver presents splendid degradation efficiency in terms of the emergence of the hydroxyl radical (˙OH) and thus oxidizes organic contaminants in wastewater.[19] Compared to conventional Fenton treatments, photo-electro Fenton processes exhibit better reactive environmental adaptability due to the self H_2O_2-production profile.[20] With the treatment of direct current (DC), gaseous oxygen (O_2) is transferred into the solution in the cathode region and continuously decomposes into two oxygen atoms for the electrochemical oxidation of H_2O_2. Whereafter, the resultant H_2O_2 can react with Fenton agents (ferrous, manganese and copper ions, customarily) to homogeneously generate superoxidized ˙OH,[21] and thus chemically oxidize the organic dyestuff pollutants to CO_2, H_2O and inorganic salts, ultimately. Meanwhile, numerous previous studies have shown that the caloric effect can stride over the energy barrier of chemical reactions and speed up the efficiencies of Fenton reactions. In consideration of the near infrared laser (NIR) driven photothermal effect of specific nanoparticles, photothermal performance designed Fenton agents can be used for enhanced Fenton degradation.[22–24]

Herein, we advance a photo-electro Fenton nanoplatform based on concave octopus-like PtCu nanoframes (COPC-Nfs).[25] Briefly, Pt atoms can mediate a typical electrooxidation to form H_2O_2, and then Cu atoms trigger a series of Fenton reactions with the assistance of H_2O_2 for further elimination of dyestuff pollution. Moreover, with NIR laser irradiation, COPC-Nfs could initiate photothermal conversion to yield high-calorie, which thus provides superior catalytic conditions.[26] Furthermore, compared to conventional iron-based Fenton agents, copper-

[a]*The 1st Affiliated Hospital, Department of Wound Repair, Engineering Research Center of Biomaterials and Medical Devices of Hainan Province, College of Emergency and Trauma, Hainan Medical University, Haikou 570100, China*

[b]*College of Medical Technology and Engineering, College of Materials Science and Engineering, The 1st Affiliated Hospital, Henan University of Science and Technology, Luoyang 471003, China*

[c]*College of Chemistry and Chemical Engineering, Key Laboratory of Natural Medicine and Immune-Engineering of Henan Province, Henan University, Kaifeng 475004, China. E-mail: sjiahua@henu.edu.cn*

† Electronic supplementary information (ESI) available. See https://doi.org/10.1039/d2na00233g

‡ These authors contributed equally to this work.

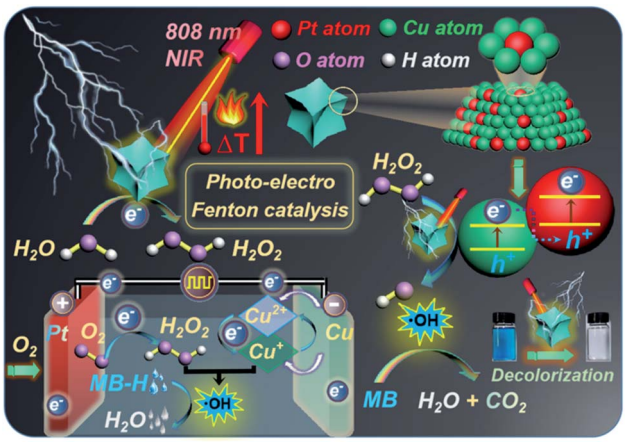

Scheme 1 Schematic illustration of MB-H degradation by PtCu nanoframe mediated photo-electro Fenton catalysis.

based Fenton catalysis reveals substantially more efficiency in neutral pH aquatic environments. In this research, methylene blue (MB-H) was selected as the model dyestuff to estimate the dye removal performance of COPC-Nfs. Scheme 1 primarily schematically displays the mechanism of degradation by using the photo-electro Fenton nanoplatform. To the best of our knowledge, this is the pioneered application for dye removal by PtCu nanoframe mediated photo-electro Fenton catalysis.

In a typical experiment, we first synthesized oleate-capped COPC-Nfs through a typical solvothermal method at 175 °C in an oil bath. Then, the oleate-free COPC-Nfs were obtained by immersion in the HCl solution (pH 4.0). The characteristic sharps of the as-designed nanoparticles were recorded at 0.5 h (Fig. 1a), subsequently at 3.0 h (Fig. 1b) and ultimately at 24 h (Fig. 1c). The oleate-free COPC-Nfs are presented in Fig. 1d. The obtained nanoframes revealed a time-dependent crystal growth behavior and showed a typical concave octopus-like morphology, eventually.

By using scanning electron microscopy (SEM, Fig. 2a) and high-angle annular dark-field scanning-transmission electron microscopy (HAADF-STEM, Fig. 2b), the octopus-like COPC-Nfs present a narrow size distribution of about 61.3 nm. The symmetric foot length of the as-synthesized COPC-Nfs is about 38.6 nm with a foot length of about 21.1 nm (Fig. S1†). The high resolution transmission electron microscopy (HRTEM) result (Fig. 2c) of COPC-Nfs showed the detailed information about the crystalloid extended along the directed [110] zone axis, and the corresponding sequential steps and terrace atoms were further observed on the surfaces of the obtained COPC-Nfs. The specific crystalline analysis further shows that the continuous stepped facets are sequentially distributed at {221}, {331}, {553} terraces (Fig. S2†), respectively. Then, the physical–chemical properties of COPC-Nf nanocatalysts were further evaluated by energy dispersive X-ray spectroscopy (EDX), X-ray diffraction analysis (XRD) and X-ray photoelectron spectroscopy (XPS) analysis. As shown in Fig. 2d, the element ratio of Pt : Cu is about 42.5 : 100. To verify the crystallography feature of the as-prepared COPC-Nfs, a typical XRD measurement was adopted as corroboration. The XRD pattern of COPC-Nfs shows a standard face-centered-cubic (FCC) Pt–Cu alloy crystallographic feature

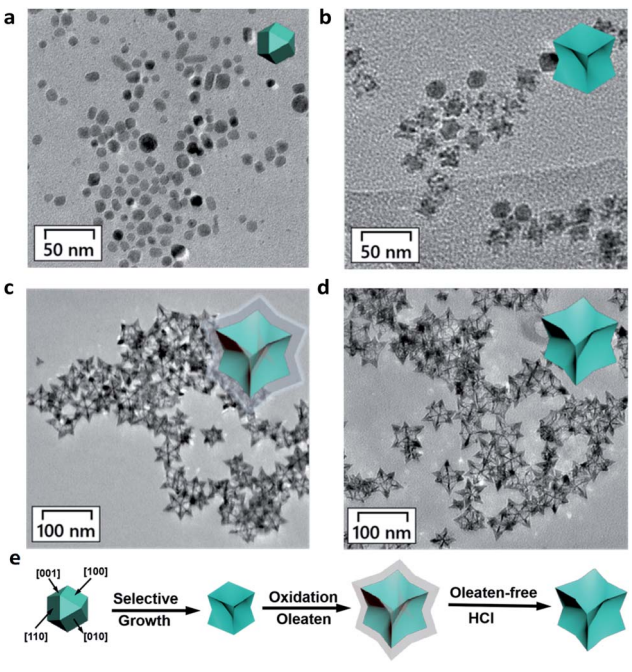

Fig. 1 Graphic TEM images for the obtained oleate-capped COPC-Nfs at different time periods of the fabrication process: (a) 0.5 h, (b) subsequent 3.0 h and (c) 24.0 h for the oleate-capped COPC-Nfs; (d) TEM images of the oleate-free COPC-Nfs; (e) scheme of COPC-Nf preparation in major steps.

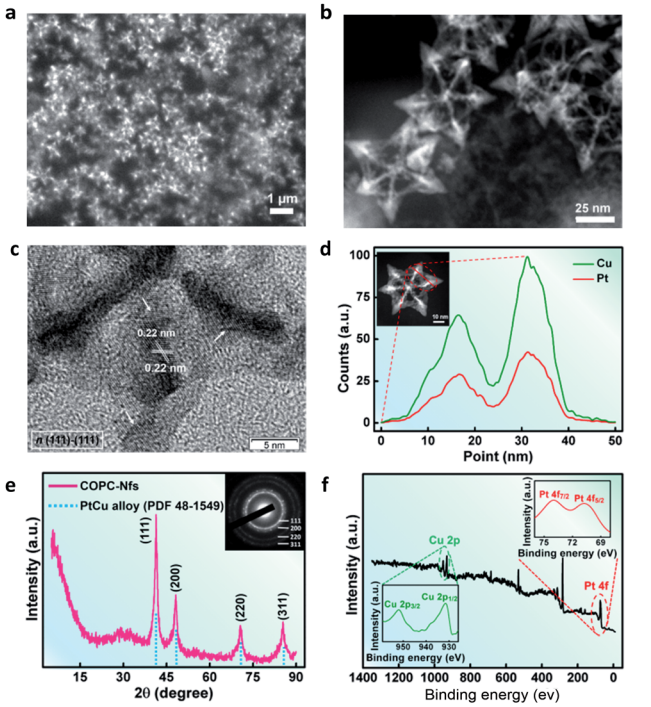

Fig. 2 (a) SEM; (b) HAADF-STEM; (c) HRTEM images of the obtained COPC-Nfs; (d) EDX line-scanning isotherm of the COPC-Nfs; (e) XRD and (f) XPS measurements of the COPC-Nfs.

(Fig. 2e). Characteristic peaks situated at $2\theta = 41.4°$, 46.7°, 70.7° and 85.3° are adjacently assigned to the (111), (200), (220), and (311) planes. Compared to the crystal spectroscopy of PtCu alloy (PDF no: 48-1549), the diffraction peaks of COPC-Nfs shift a little (about 0.2°), which was attributed to the high content of the copper element in the nanocatalyst.

The consequential XPS test further verifies the alloying behavior of Pt elements and Cu elements in the COPC-Nfs. Typically, peaks at 71.2 and 74.4 eV are for Pt 4f7/2 and Pt 4f5/2, and peaks arising at 932.3 and 953.0 eV are assigned to Cu 2p1/2 and Cu 2p3/2 (Fig. 2f and S3†).

H_2O_2 is the most important factor in a typical Fenton reaction. To verify the electric field-triggered H_2O_2 generation profile of the as-synthesized COPC-Nfs, we first detected the H_2O_2 production at 10.0 mA DC. An interesting phenomenon was found that the addition of Cl^- ions could eventually hasten the output of H_2O_2 (Fig. 3a), and the time-dependent production presented a current strength-corresponding behavior within the electrocatalytic process (Fig. 3b). pH is another principal factor of the Fenton reaction. Interestingly, after a 30 minute electrocatalytic reaction, the pH of the solution decreased to about 4.8 (Fig. 3c), which is an appropriate pH range for Fenton catalysis. On the one hand, as the third key factor of the Fenton reaction, the Cu ion concentration was further measured at a series of current intensities (Fig. 3d). All these three elements would ensure the facilitation of the Fenton reaction. The formation of ˙OH was further monitored in this study. As presented in Fig. 3e, compared to the control groups, the COPC-Nfs presented the superior generation of ˙OH with the assistance of Cl ions at 10 mA DC, which indicates that the COPC-Nfs could readily mediate a representative electro Fenton reaction to trigger off ˙OH. The formation mechanism of ˙OH and potential dye degradation are shown in Fig. 3f.

It is well-known that temperature can significantly promote the rate of reaction. Therefore, this phenomenon gives us a possibility to develop a calorie-aided Fenton discoloration strategy for dye elimination. COPC-Nfs display very good absorptiometric capacity (Fig. S4†) and excellent photothermal performance, and is preferred to be used as a good choice for dye decoloration. When irradiated with an 808 nm NIR laser (5 min, 2.0 W cm^{-2}), COPC-Nfs (300 μg mL^{-1}) can produce a high temperature of over 50 °C (Fig. 4a and b). We detected the surface charge of the COPC-Nfs in various states. As presented in Fig. S5,† the COPC-Nf nanoparticles display electronegativity in the degradation process. Meanwhile, the degradation of MB-H at different pH was measured, as shown in Fig. S6,† and there was no significant difference between various pH. We further detected the dye degradation efficiency by treating with DC (10.0

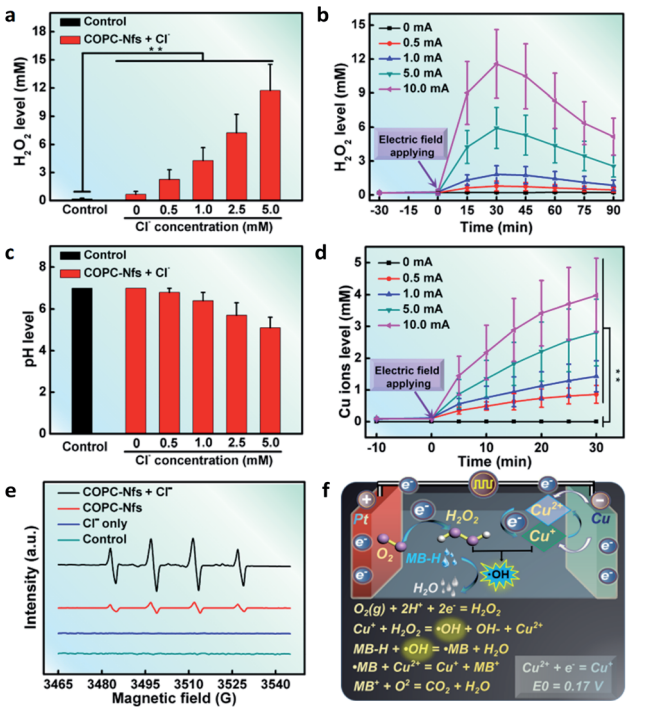

Fig. 3 H_2O_2 generation profiles under various Cl^- concentrations (a) and different current intensities (b) by COPC-Nfs (300 μg mL^{-1}); (c) pH status after 30 min of electrification; (d) Cu ion release by using an electric field; (e) ESR spectra of ˙OH accumulation; (f) schematic diagram of the self-generation of ˙OH.

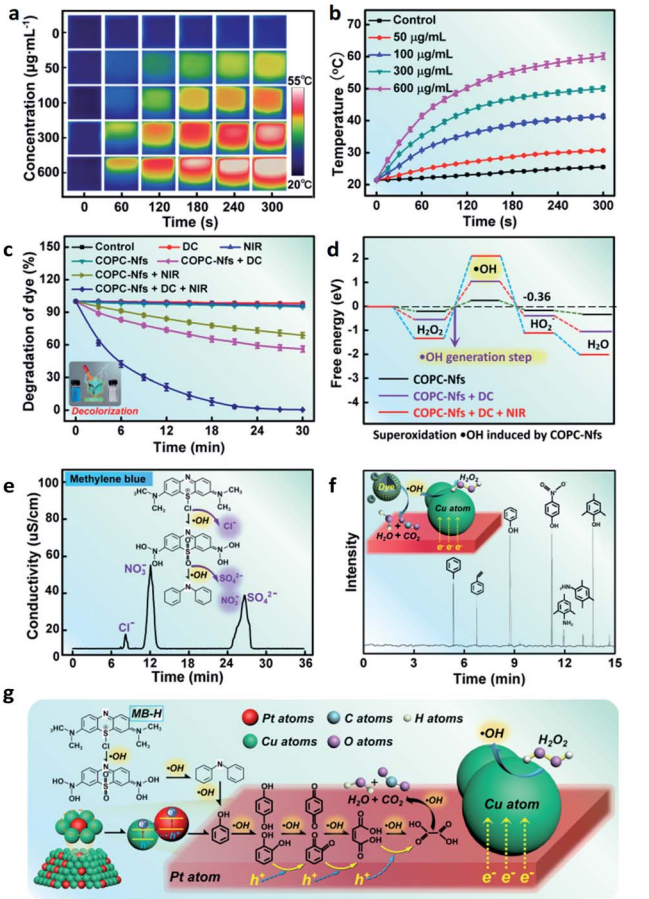

Fig. 4 (a) Infrared thermography image and (b) concentration-dependent exotherm of COPC-Nfs; (c) degradation efficiency for MB-H (10.0 mg L^{-1}) by different treatments; (d) DFT calculations of ˙OH production; (e) determination of inorganic ions and (f) GC-mass spectra of the dye degradation process; (g) schematic illustration of MB-H degradation by using COPC-Nfs.

mA, 15.0 W) and NIR alone and using them together. COPC-Nfs irradiated with DC and NIR show much higher degradation efficiency (Fig. 4c and S7†). Whereafter, typical DFT calculations were used to verify the inducement of high degradation by using the COPC-Nf nanocatalyst, as shown in Fig. 4d. COPC-Nfs can vastly enhance the output of $^{\bullet}OH$ with the combined utilization of DC and the NIR laser. After 40 min of degradation, MB-H can be progressively resolved into ions such as Cl^{-}, NO^{3-} and SO_4^{2-}during the Fenton catalytic process (Fig. 4e). A GC-MS measurement was taken to assess the intermediate products during the treatment procedure. As shown in Fig. 4f, MB-H was finally degraded into multiple small molecular substances such as methylbenzene, trimethylphenol, styrene, 4-amino-thiophenol, *p*-nitrophenol and phenol by COPC-Nfs accordingly. Next, a total organic carbon (TOC) measurement was adopted to further confirm the end-product of the photo-electro Fenton catalysis. The loss in TOC (43.7%, Fig. S8†) of organic substances could be identified as due to the CO_2 generation. The conceivable degradation approach of MB-H is credibly presented in Fig. 4g. Furthermore, the reusable performance of COPC-Nfs is shown in Fig. S9;† after 10 times of reuse, the nanoagents still reveal high activity (over 95%), which means excellent reusable performance for dye elimination. The H_2O_2 generation profiles were further monitored for different nanocatalysts under DC treatment, and the result is shown in Fig. S10.† Compared to the commonly used TiO_2 and Pt nanoparticles (Pt-Nps), COPC-Nf nanoagents reveal higher productivity, obviously. Subsequently, we contrast the degradation performance between the most common photo-catalysts. The obtained results are shown in Tables S1 and S2.† COPC-Nf nanocatalysts display higher degradation efficiency within less time. As it turns out, all the results reveal that COPC-Nfs have excellent capacity for photo-electro Fenton catalytic dye elimination.

In conclusion, we have developed a photo-electro Fenton catalytic nanoplatform based on concave octopus-like PtCu nanoframes with photothermal capability. The ESR and DFT measurements manifested that the dye elimination process was attributed to the photo-electro Fenton catalysis procedure. The nanoagents show excellent Fenton catalytic performance by H_2O_2 self-aggregation, Cu ion enrichment and acid pH achievement. By treating with a 10.0 mA DC electric field, the COPC-Nfs nanocatalyst exhibited an extraordinarily high degradation efficiency for dye removal. Meanwhile, the photothermal conversion performance of COPC-Nfs under NIR laser irradiation could enormously enhance the eventual catalytic efficiency of the COPC-Nf mediated Fenton-like process. Furthermore, the addition of Cl^{-} ions could greatly enhance the catalytic efficiency of the photo-electro Fenton catalytic process. All these results show that the reusable COPC-Nf Fenton-like nanocatalyst has great potential for dye wastewater management.

Conflicts of interest

There are no conflicts to declare.

Acknowledgements

This work was supported by the National Natural Science Foundation of China (No. 31800836, 81860347 and 12104134), China Postdoctoral Science Foundation (No. 2020M682285), Innovation Talents Project of Colleges and Universities in Henan Province (No. 21HASTIT046), Hainan Provincial Health and Family Planning Commission Project (21A200062), and Hainan Province Science and Technology Special Fund (ZDYF2021SHFZ238 and ZDKJ2021038).

Notes and references

1 X. Y. Wang, Y. Ma, Q. M. Wu, Y. Q. Wen and F. S. Xiao, *Chem. Soc. Rev.*, 2022, **51**, 2431–2443.
2 X. Wu, Y. Chen and Y. Liu, *Adv. Sustainable Syst.*, 2019, **5**(3), 1800165.
3 N. Mohammed, N. Grishkewicha and K. C. Tam, *Environ. Sci. Nano*, 2018, **5**, 623–658.
4 J. M. Serrano, A. U. Khan, T. Y. Liu, Z. Xu, A. R. Esker and G. L. Liu, *Adv. Mater. Interfaces*, 2020, **16**(7), 202000507.
5 S. Chongdar, S. Bhattacharjee, P. Bhanj and A. Bhaumik, *Chem. Commun.*, 2022, **58**, 3429–3460.
6 L. Y. Jing, Q. Tian, P. P. Su, H. T. Li, Y. Zheng, C. Tang and J. Liu, *J. Mater. Chem. A*, 2022, **10**, 4068–4075.
7 L. Valencia, S. Kumar, E. M. Nomena, G. Salazar-Alvarez and A. P. Mathew, *ACS Appl. Nano Mater.*, 2020, **3**(7), 7172–7181.
8 S. D. Sun, X. J. Yu, Q. Yang, Z. M. Yang and S. H. Liang, *Nanoscale Adv.*, 2019, **1**, 34–63.
9 G. D. Gawande, D. V. Pinjari and P. V. Chavan, *Chem. Eng. Tech.*, 2022, 202100419.
10 C. Y. Toe, C. Tsounis, J. J. Zhang, H. Masood, D. Gunawan, J. Scott and R. Amal, *Energy Environ. Sci.*, 2021, **14**, 1140–1175.
11 X. K. Zeng, Y. Liu, X. Y. Hua and X. W. Zhang, *Green Chem.*, 2021, **23**, 1466–1494.
12 M. R. Li, X. Qin, M. X. Gao, T. H. Li and Y. Lv, *Environ. Sci.: Nano*, 2022, **9**, 632–652.
13 W. Razzaq, C. Serra and D. Chan-Seng, *Chem. Commun.*, 2022, **58**, 4619–4622.
14 C. Zhang, B. H. Wu, M. Q. Ma, Z. K. Wang and Z. K. Xu, *Chem. Soc. Rev.*, 2019, **48**, 3811–3841.
15 L. Chandra, K. Jagadish, V. Karthikeyarajan, M. Jalalah, M. Alsaiari, F. Harraz and R. Balakrishna, *ACS Omega*, 2022, **7**(11), 9674–9683.
16 S. Chowdhury, A. Al-Mamun, M. Zulfiqar, M. M. Alam and M. M. Rahman, *ChemistrySelect*, 2022, **3–4**(62), 296–309.
17 B. H. Tang, J. T. Zhao, Y. Jiao, J. F. Xu and X. Zhang, *Chem. Commun.*, 2019, **55**, 14127–14130.
18 X. W. Da, D. J. Tang, L. Wang and J. H. Ma, *Environ. Sci.: Water Res. Technol.*, 2020, **6**, 515–522.
19 G. A. Coppola, S. Pillitteri, E. V. V. Eycken, S. L. You and U. K. Sharma, *Chem. Soc. Rev.*, 2022, **51**, 2313–2382.
20 B. W. Zhong, H. L. Huang, X. Jing and C. Y. Duan, *Chem. Commun.*, 2022, **58**, 3961–3964.
21 J. H. Li, J. B. Zhang, X. B. Jiao, J. H. Shi, J. X. Ye, K. N. Song, J. F. Bao, G. D. Li and K. Lei, *J. Alloy. Compd.*, 2022, **895**, 162624.

22 T. Y. Su, G. P. Lu, K. K. Sun, M. Zhang and C. Cai, *Catal. Sci. Technol.*, 2022, **12**, 2106–2121.
23 A. T. Maha and A. M. Shehab, *Nanoscale Adv.*, 2019, **1**, 1362–1371.
24 F. Ganjali, A. Kashtiaray, S. Zarei-Shokat, R. Taheri-Ledari and A. Maleki, *Nanoscale Adv.*, 2022, **4**, 1263–1307.
25 J. M. Zhai, J. P. Gao, J. B. Zhang, D. C. Liu, S. G. Gao, Y. Y. Yan, K. K. Zhang, K. Y. Cai, F. B. Yu, M. P. Lin and J. H. Li, *Chem. Eng. J.*, 2022, 136172.
26 T. X. Zhang, T. Wang, F. L. Meng, M. Q. Yang and S. Kawi, *J. Mater. Chem. C*, 2022, **10**, 5400–5424.